MoS_2/Graphene Composite Paper for Sodium-Ion Battery Electrodes

Lamuel David, Romil Bhandavat, and Gurpreet Singh*

Mechanical and Nuclear Engineering Department, Kansas State University, Manhattan, Kansas 66506, United States

ABSTRACT We study the synthesis and electrochemical and mechanical performance of layered free-standing papers composed of acid-exfoliated few-layer molybdenum disulfide (MoS_2) and reduced graphene oxide (rGO) flakes for use as a self-standing flexible electrode in sodium-ion batteries. Synthesis was achieved through vacuum filtration of homogeneous dispersions consisting of varying weight percent of acid-treated MoS_2 flakes in GO in DI water, followed by thermal reduction at elevated temperatures. The electrochemical performance of the crumpled composite paper (at 4 mg cm^{-2}) was evaluated as counter electrode against pure Na foil in a half-cell configuration. The electrode showed good Na cycling ability with a stable charge capacity of approximately 230 mAh g^{-1} with respect to total weight of the electrode with Coulombic efficiency reaching approximately 99%. In addition, static uniaxial tensile tests performed on crumpled composite papers showed high average strain to failure reaching approximately 2%.

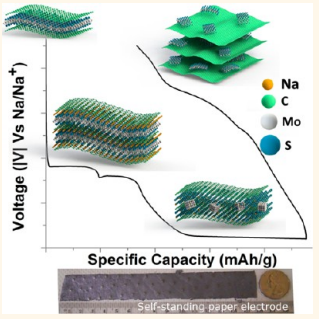

KEYWORDS: TMDC · sodium battery · free-standing electrode · graphene · MoS_2

Lithium-ion batteries (LIBs) have been extensively studied for energy-storage applications like portable electronic devices and electric vehicles.[1−3] However, concerns over the cost, safety, and availability of Li reserves[4] for large-scale applications involving renewable energy integration and electrical grid have to be answered. In this regard, sodium-ion batteries (SIBs) have drawn increasing attention because, in contrast to lithium,[5−7] sodium resources are practically inexhaustible and evenly distributed around the world while the ion insertion chemistry is largely identical to that of lithium. Also, from an electrochemical point of view, sodium has a very negative redox potential (−2.71 V *vs* SHE) and a small electrochemical equivalent (0.86 gA h^{-1}), which make it the most advantageous element for battery applications after lithium. However, many challenges remain before SIBs can become commercially competitive with LIBs. For instance, Na ions are about 55% larger in radius than Li ions, which makes it difficult to find a suitable host material to allow reversible and rapid ion insertion and extraction.[8]

To this end, researchers have proposed a number of high-capacity sodium host materials (negative electrode) involving either carbon or group IVA and VA elements that form intermetallic compounds with Na.[9−13] The alloying compounds demonstrate high first cycle Na-storage capacities, such as $Na_{15}Sn_4$ (847 mAh g^{-1}), $Na_{15}Pb_4$ (485 mAh g^{-1}), Na_3Sb (600 mAh g^{-1}), and Na_3P (2560 mAh g^{-1}). However, this comes at the cost of very high volume change upon Na insertion (as much as 500% in some cases), resulting in formation of internal cracks, loss of electrical contact, and eventual failure of the electrode (particularly for thick electrodes).[14] Novel nanostructured designs that can accommodate large volumetric strains need further exploration.[15−18] For carbon-based electrode materials, much of the emphasis has been on hard carbons due to large interlayer spacing and disordered structure.[19−25] For example, hard carbon prepared from pyrolyzed glucose, carbon black, and carbon microspheres has been shown to exhibit initial reversible capacities of 300, 200, and 285 mAh g^{-1}, respectively, in a Na-ion cell.[15−17] More recently, another hard carbon material that could deliver a reversible capacity of more than 200 mAh g^{-1} over 100 cycles has been reported.[22,25] However, these studies were conducted on traditional anode architecture (prepared through slurry coating of active material on metallic current collector foil, and the capacities reported were with respect to the active material only), either at low cycling current rates or at elevated temperatures. Overall,

* Address correspondence to gurpreet@ksu.edu.

Received for review November 29, 2013 and accepted January 21, 2014.

Published online January 21, 2014
10.1021/nn406156b

new electrode design and concepts based on chemistry other than alloying and ion intercalation must also be explored to realize improved performance in Na-ion batteries under normal operating conditions.

Studies on Li-ion batteries have shown that 2-D layered nanomaterials such as graphene and transition metal dichalcogenides (TMDCs *e.g.*, MoS_2 and WS_2) are promising materials for efficient storage and release of Li ions.[26−37] However, when compared with graphite, the electrochemical lithiation in layered TMDCs is distinct as majority of the lithium is stored by means of a conversion reaction in which Li ion reacts with the TMDC forming Li_2S and transition metal phases as the reaction products. More important, this type of a conversion reaction can allow transfer of 2−6 electrons per transition metal compared to a single electron in the case of an intercalation reaction (lithium/carbon system).[1,34] Although layered graphite has been ruled out for sodium-based systems (as Na ions do not tend to form staged intercalation compounds with graphite),[38−40] a graphene-based free-standing paper-based electrode can provide a porous and flexible support structure for a TMDC to undergo a reversible conversion-type reaction with Na ions. It can also act as an efficient electronic current collector, thereby eliminating the need for a metallic substrate (generally a 10 μm thick foil at 10 mg cm^{-2}),[41,42] electrically conducting additives, and polymeric binders that amount to a total of approximately 10% of the cell weight[42] in traditional negative electrodes.[43−48] Herein, we provide the first report of (a) synthesis of composite papers from acid-functionalized MoS_2 and reduced graphene oxide flakes, (b) improved capacity and high efficiency reversible Na storage in the self-standing flexible MoS_2/graphene electrodes at room temperature, and (c) mechanical characterization that highlights the high strain to failure in these composite papers.

RESULTS AND DISCUSSION

Layered "as-obtained" MoS_2 was exfoliated by mechanical sonication in chlorosulfonic acid followed by quenching in DI water (see Methods, Materials, and Instrumentation section). A digital image of the acid-treated MoS_2 dispersion immediately after quenching in DI water is shown in Figure 1a. From SEM observations, the particle size for MoS_2-raw was observed to be approximately 20−40 μm (Figure 1b), while that of MoS_2-SA was less than 20 μm (Figure 1c). Shown in Figure 1d−f are high-magnification TEM images of acid-treated MoS_2 sheets. All of the sheets were observed to be only a few layers thick with flake size ranging from 100 nm to 1 μm. From literature, we can correlate the reason for exfoliation of MoS_2 to electrostatic repulsion forces caused by protonation of MoS_2 surfaces.[50] Using DLVO theory, ζ-potential measurements can quantify this surface charge on MoS_2 sheet and hence help in establishing the dispersion stability. For ζ-potential measurements, the pH was varied by adding 0.01 M NaOH solution, and since the contribution from dissociated OH^- ions in the measured potential is minimal, it was neglected in the analysis. The lower pH range was limited to protect the instrument electrode. The surface potential showed a range varying from −35 mV at pH 4 to −60 mV at pH 10, shown as an inset in Figure 1g. As higher surface potential (negative) implies more stable suspensions, based on the obtained results, higher pH suggests a larger exposed MoS_2 sheet surface. This dependence of surface potential on pH is similar to that observed for exfoliated (surface-functionalized) graphene sheets by Coleman's group.[51] Further, we utilize their model for graphene stabilization mechanism to explain the superacid−MoS_2 interaction mechanism (see Supporting Information).[51,52] Figure 1g is the plot for total interaction energy per unit area of the sheet (V_T/A).

Further analysis involved Raman spectroscopy and X-ray diffraction before and after acid treatment. Raman spectrum (Figure 1h) obtained by use of 633 nm wavelength laser showed typical $E_{2g}{}^1$, A_{1g}, 2LA(M), and A_{1g}+LA(M) peaks at 380, 407, 460, and 641 cm^{-1}, respectively. The in-plane $E_{2g}{}^1$ peak results from opposite vibration of two S atoms with respect to the Mo atom, while the A_{1g} peak is associated with the out-of-plane vibration of only S atoms in opposite directions.[53,54] The intensity of A_{1g} peak arises from the resonance Raman (RR) scattering because the incident laser is in resonance with the direct band gap (~1.96 eV) at the K point. The asymmetric 2LA(M) peak is associated with second-order zone-edge phonon (LA(M)) and a first-order optical phonon peak (A_{2u}).[55−58] These results along with electron microscopy results suggest that the structure is relatively undistorted MoS_2.[59,60] Further, X-ray diffraction analysis (XRD) of MoS_2-raw and MoS_2-SA in Figure 1i showed distinct peak at 14.3 and 13.97° 2θ, respectively. These peaks are associated with 002 reflection from the basal plane of MoS_2 with measured "*d*" spacing of 3.1 and 3.2 Å lattice plane of hexagonal MoS_2 (JCPDS #37-1492). This suggests restacking of the MoS_2 layers upon drying.[61,62]

Later, the MoS_2/rGO papers were prepared by vacuum filtration of graphene oxide (GO) and molybdenum disulfide (MoS_2) sheets dispersed in water/isopropyl alcohol (1:1) solution, which is shown with the help of a schematic in Figure 2a, while Figure 2b is the digital image of one such paper synthesized using this technique. SEM images in Figure 2c,d and Supporting Information Figure S1a−h show the top-view and corresponding cross-section view of 60MoS_2, rGO, 20MoS_2, 40MoS_2, and 60MoS_2-raw free-standing papers, respectively. The papers were approximately 10−20 μm in thickness (that varied with the weight percentage of MoS_2 in GO) with a relatively homogeneous

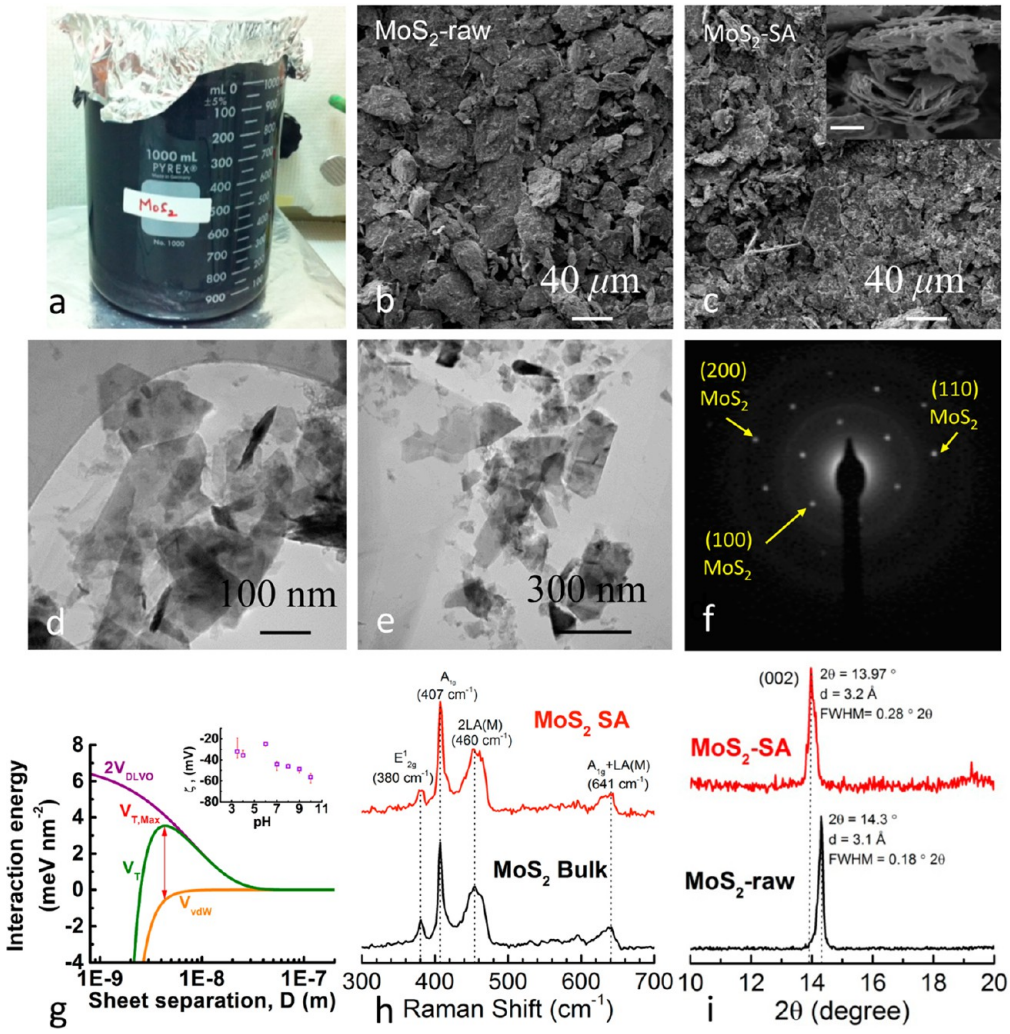

Figure 1. (a) Photographic image showing acid-treated MoS_2 immediately after it was quenched in 1 L of DI water at a concentration of approximately 2 mg mL^{-1}. SEM images showing the structure and size distribution of MoS_2 (b) before and (c) after superacid treatment. The particle size varied between 20 and 40 μm and approximately 1 and 20 μm for raw and acid-treated MoS_2, respectively. The scale bar in the inset is 2 μm. (d,e) High-resolution TEM image of superacid-treated MoS_2 (MoS_2-SA) sheets. (f) SAED pattern corresponding to TEM image in (e). (g) Graph showing calculated total interaction potential energy (V_T), repulsion (V_{DLVO}), and attraction energy (V_{vdW}) (per unit area) with increasing MoS_2 sheet separation distance (log scale). Inset: Experimentally measured ζ-potential, showing better dispersion stability at higher pH values. (h) Raman spectra of MoS_2 before and after acid treatment. The similarity in the relative intensity and position of the $E_{2g}{}^1$ and A_{1g} peaks suggests that the structure was largely undistorted MoS_2. (i) Change in intensity and fwhm of MoS_2 peak at 14° 2θ in the XRD spectra suggests increase in MoS_2 interlayer distance after the acid treatment (JCPDS #37-1492).

composition (see Supporting Information Figure S2 for high-resolution image). The interleaved structure observed in the cross-sectional images is preferred for easy storage and release of larger Na ions, particularly at higher current densities or *C* rates. The digital photograph in the inset of Supporting Information Figure S1a–d confirms the outstanding structural flexibility of rGO and MoS_2/graphene specimens. Further analysis involved SEM-X-ray energy-dispersive spectroscopy (EDX), shown in the inset in Figure 2c. The EDX spectra from spot 1 (square) showed peaks at 0.27 and 0.52 keV, which correspond to carbon (85.43 atom %) and oxygen (10.41 atom %) Kα energy, respectively. The low oxygen content indicates that rGO was highly reduced and pristine. In addition to carbon and oxygen, two small peaks at 2.29 and 2.3 keV corresponding to molybdenum Lα (1.39 atom %) and sulfur Kα (2.78 atom %) energy, respectively, were also observed. At spot 2, peaks corresponding to Mo (26.13 atom %) and S (46.48 atom %) were prominent when compared to that of carbon (24.39 atom %), which unambiguously confirms the presence of MoS_2 sheets in the composite. TEM images are shown in Figure 2e and Supporting Information Figure S1i–l. It is clear that the rGO sheets were layered with few layers of MoS_2 forming a very good electron conductive layer and also a support structure for free-standing paper. The inset in Figure 2e is the selected area electron diffraction (SAED) pattern that indicates a multiple spot pattern, one of which is due to the polycrystallinity of restacked

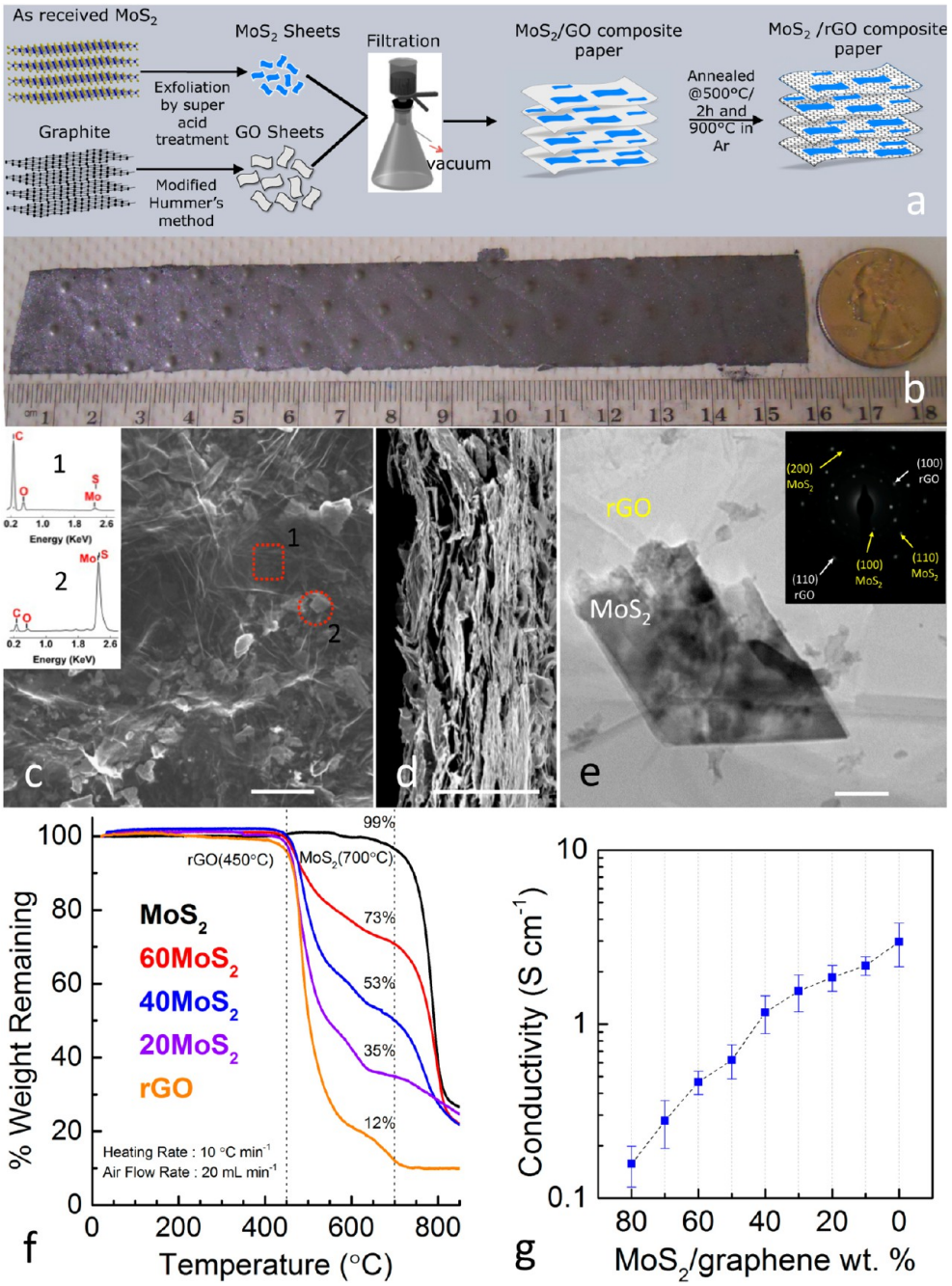

Figure 2. (a) Schematic representation showing synthesis of rGO/MoS_2 composite paper. (b) Digital picture showing large-area composite paper prepared through vacuum filtration. (c) SEM top-view image of 60MoS_2 paper; inset shows the EDX spectra of spots in the SEM image indicating the material to be rGO (square) and MoS_2 (circle). The scale is 10 μm. (d) Corresponding SEM cross-sectional images show the morphology of the paper. Average thickness of this paper was observed to be ~20 μm. (e) TEM image and SAED pattern of 60MoS_2. The MoS_2 sheets are observed to be wrapped by much larger graphene sheets. In SAED pattern (inset), multiple spot patterns are observed, one of which is due to the polycrystallinity of restacked rGO sheets while a second set of spot patterns is assigned to MoS_2 sheets. The scale is 100 nm. (f) Thermogravimetric analysis data for MoS_2-SA, MoS_2-rGO composite paper, and rGO paper. (g) Graph of electrical conductivity *vs* MoS_2 loading in the composite paper.

rGO sheets, while a second set of spot patterns was due to MoS_2 sheets. The hexagonal spot pattern (inset of Supporting Information Figure S1i) indicates that the graphitic AB stacking was preserved in the lattice after thermal reduction. To further observe the distribution of MoS_2 in the composite, EDX elemental mapping was performed on the cross section of the 60MoS_2 specimen (Supporting Information Figure S3). A slightly higher percentage of elemental carbon (graphene) was observed on one end of the paper, which is somewhat typical in a high inclusion content (in this case, MoS_2 in graphene) matrix.[63] Supporting Information Table S1 summarizes the percentage of each element detected in the corresponding EDX map.

Further evidence showing the presence of MoS_2 in rGO was achieved through X-ray photoelectron spectroscopy (XPS) (Supporting Information Figure S4) that compares powered MoS_2-SA with $60MoS_2$ paper before and after reduction. MoS_2 peaks that were present in the starting material were also present in the free-standing paper. Notable change was observed in the intensity of oxygen (O1s) and carbon (C1s) peaks for the $60MoS_2$ specimen (before and after reduction) due to addition of GO. Raman spectroscopy of $60MoS_2$ paper (Supporting Information Figure S5) showed typical MoS_2 peaks at 373 ($E_{2g}{}^1$), 400 (A_{1g}), and 445 (2LA(M)) cm^{-1} along with characteristic rGO D and G peaks at 1330 (D) and 1560 (G) cm^{-1}, respectively. X-ray analysis (Supporting Information Figure S6) of $60MoS_2$ paper also confirmed the presence of rGO (JCPDS #01-0646) and MoS_2 (JCPDS #37-1492) in the composite. Further, the exact amount of MoS_2 in the final composite paper (after reduction) was inferred by carrying out thermogravimetric analysis (TGA) in flowing air. As can be seen in Figure 2f, rGO and MoS_2 had oxidation events at approximately 450 and 700 °C, respectively. From the TGA data, it was observed that thermally reduced $60MoS_2$, $40MoS_2$, and $20MoS_2$ papers had approximately 73, 53, and 35 wt % of MoS_2 in rGO.

Later, the effect of change in filler concentration on electrical conductivity of the composite was studied by use of a four-point measurement technique, which is presented in Figure 2g. The increase in conductivity with increasing rGO concentration in the composite was somewhat nonlinear. This type of behavior is typical when electrically insulating filler (MoS_2) is added to a relatively conducting matrix (rGO) because significant increase in conductivity can only occur after the first conducting path through the sample is formed.[64,65]

Electrochemical Performance. Supporting Information Figure S7 depicts the voltage charge/discharge and differential capacity curves for various paper electrodes with varying MoS_2 content. Supporting Information Figure S7a shows the voltage profiles of rGO for the first and second cycle. The first cycle discharge and charge capacities were 784 and 86 mAh g^{-1}. The differential capacity profiles in Supporting Information Figure S7b show a primary reduction peak at 200 mV, a secondary reduction peak at 610 mV, and a weak oxidation peak at 0.9 V. The peak at 200 mV, which is present in all subsequent cycles, is associated with intercalation of rGO, while the peak at 610 mV suggests formation of a solid electrolyte interphase (SEI) layer, which exists only in the first cycle. Supporting Information Figure S7c,d shows the initial charge/discharge voltage profile and differential capacity curves for the $20MoS_2$ electrode. In the first cycle, there are three reduction peaks. A peak at 150 mV is attributed to MoS_2/rGO intercalation, while those at 580 mV and 0.8 V are attributed to SEI formation in rGO and MoS_2, respectively, as these were present only during the first cycle. Only one subtle anodic peak at 1.35 V was observed. As the percentage of MoS_2 increased from 40% (Supporting Information Figure S7e,f) and 60% (Figure 3a,b), the domination of Na intercalation in MoS_2 over rGO increased, which was evidently seen with an increase in the intensity of the reduction peak at around 0.8 and 0.9 V in the first cycle (peak at 580 mV observed in rGO electrode was relatively absent). In the case of the $60MoS_2$-raw (Supporting Information Figure S7g,h) electrode, similar peaks to that of $60MoS_2$ were observed.

Later, reaction kinetics of rGO and $60MoS_2$ electrodes were compared by performing galvanostatic intermittent titration (GITT) cycling and calculating the reaction resistance to Na insertion and extraction for the two electrodes. For rGO electrodes (Supporting Information Figure S8a,c,e), the reaction resistance for Na insertion was observed to be fairly constant at ~10 Ohm g (or less) while it increased exponentially to ~50 Ohm g in the case of Na extraction at an extraction voltage of ~1.25 V. For the MoS_2 electrode (Supporting Information Figure S8b,d,f), reaction resistance increased gradually to ~20 Ohm g during Na insertion. However, for the extraction half, the resistance remained stable at ~20 Ohm g until approximately 2.5 V and then saw a sudden increase reaching ~50 Ohm g. The sudden increase in reaction resistance could be attributed to successive stage transformation processes during sodiation/desodiation or lithiation/deliathiation observed in layered intercalation compounds.[66] Interestingly, both the electrodes showed a reaction resistance value of ~10 Ohm g during initial insertion (discharge) in the upper voltage range of 2 to 1.0 V (Supporting Information Figure S8c,d). This suggests that the initial Na insertion in $60MoS_2$ composite electrode in the upper voltage range could be an intercalation reaction, which is later followed by a conversion-type reaction in the lower voltage range (indicated by rise in resistance).

Figure 3c shows the charge capacities and Coulombic efficiency of rGO, $20MoS_2$, $40MoS_2$, $60MoS_2$, and $60MoS_2$-raw anodes cycled at a constant current density of 25 mA g^{-1}. For rGO, the charge capacity was stable at ~70.5 mAh g^{-1} in the 20th cycle, while the high irreversible first cycle capacity is attributed to electrochemical reaction contributing to SEI layer formation. In the case of rGO/MoS_2 composite electrodes, the first cycle charge capacity increased with increasing percentage of MoS_2 in the composite, that is, $20MoS_2$, $40MoS_2$, and $60MoS_2$ showed 139 , 263, and 338 mAh g^{-1}, respectively. After initial drop in the capacity, rGO/MoS_2 composite electrode remained constant at 123, 172, and 218 mAh g^{-1} for $20MoS_2$, $40MoS_2$, and $60MoS_2$, respectively. $60MoS_2$ anode was the best performing with 83% capacity retention and approximately 98% average efficiency. The MoS_2-raw electrode showed a first cycle charge capacity of

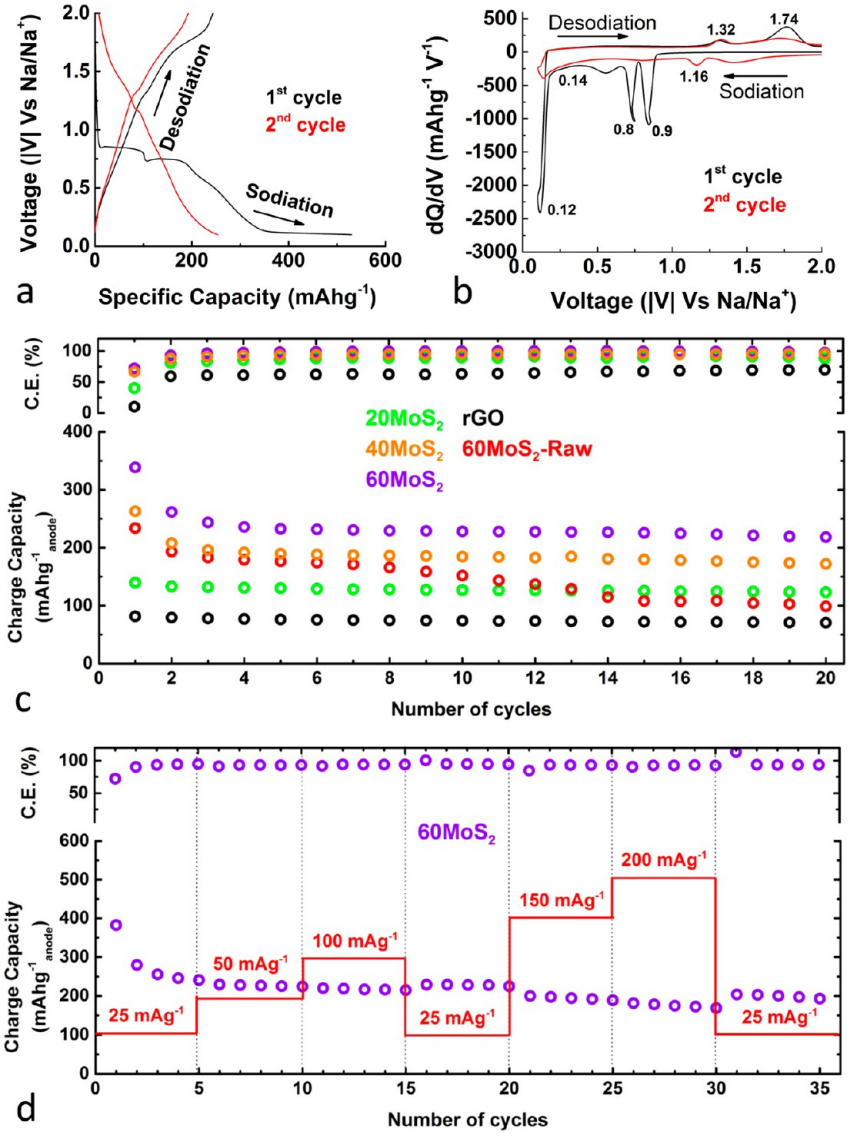

Figure 3. (a) Voltage profile of $60MoS_2$ free-standing electrode along with its corresponding (b) differential capacity curves for the first two cycles. (c) Sodium charge capacity of various electrodes at a constant current density of 25 mA g^{-1}. (d) Sodium charge capacity and corresponding Coulombic efficiency of $60MoS_2$ electrode cycled at varying current densities.

233 mAh g^{-1} that reduced to below ~100 mAh g^{-1} after 20 cycles. For the MoS_2-raw electrode, it is possible that the formation of SEI with successive cycles (and unexfoliated nature of the flakes) may have hindered the diffusion of Na into the bulk of the specimen, resulting in capacity fading on consecutive cycling. For the acid-treated MoS_2-SA electrode, the more open and interleaved structure enabled it to utilize the entire bulk of the material in the electrode, resulting in exceptional cyclic stability. Presence of conducting graphene sheets further provided the necessary platform on which volume or morphology changes due to conversion reaction could occur without any breakdown in the electrical contact.

Later, the composite paper electrode with maximum possible MoS_2 loading (*i.e.*, 90% MoS_2 in rGO) was cycled under similar conditions (Supporting Information Figure S9). However, these papers were very brittle and required special handing during cell assembly. The first cycle discharge and charge capacities were observed at 943 and 347 mAh g^{-1}, respectively. Even though the first charge capacity was higher than that of other composite electrodes, the electrode started to show random spikes in the voltage profile with a capacity drop after the second cycle. Therefore, rate capability tests were only performed on the best performing electrode specimen (*i.e.*, $60MoS_2$). As shown in Figure 3d, the electrode stabilized to a charge capacity of 240 mAh g^{-1} at a current density of 25 mA g^{-1} (with respect to total weight of the electrode) after the initial five cycles. The charge capacity remained stable (214 mAh g^{-1}, 90% retention) even at current densities as high 100 mA g^{-1}. The electrode regained most of its charge capacity (230 mAh g^{-1}, 96% retention) when

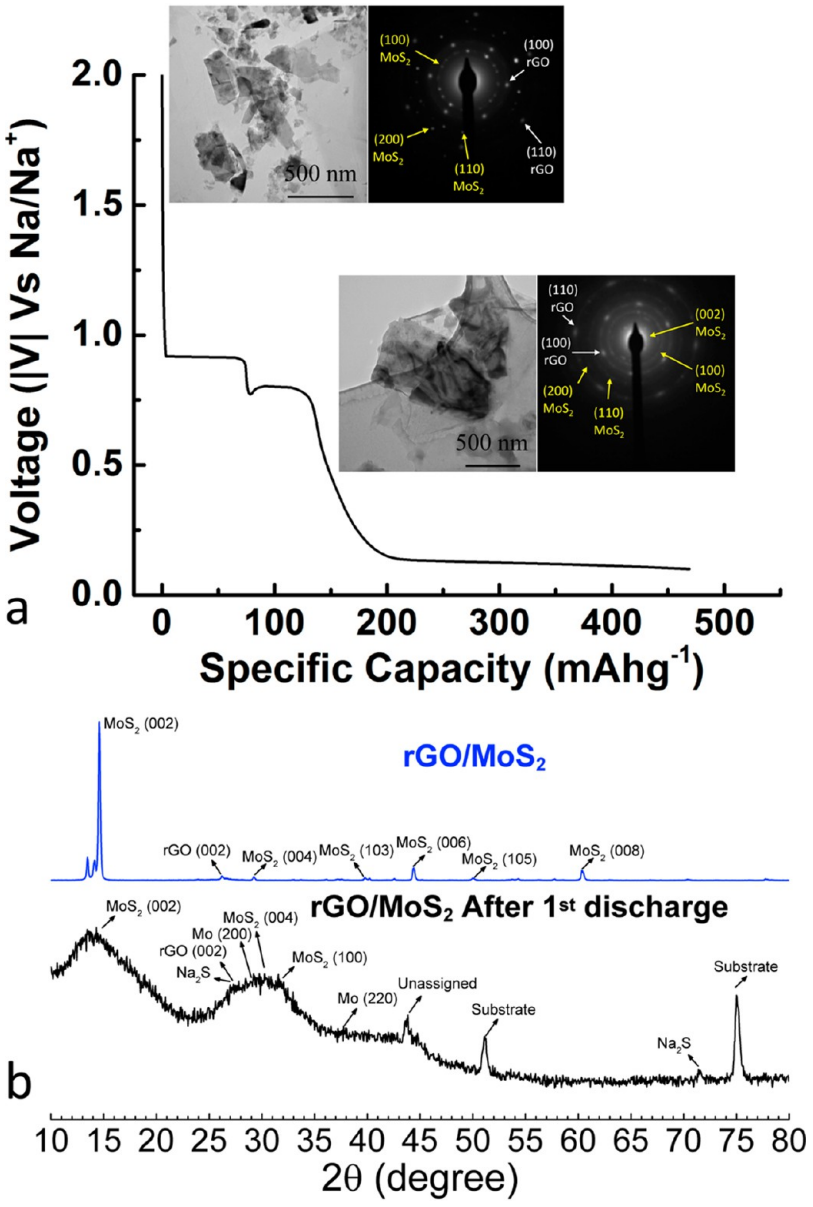

Figure 4. (a) TEM images and corresponding SAED patterns of 60MoS_2 electrode before and after first discharge cycle (0.01 V). The ring-like SAED pattern suggests formation of nanocrystallites or amorphization of MoS_2 in the sodiated (discharged) electrode.[67,68] (b) XRD pattern of 60MoS_2 electrode before and after first discharge cycle (0.01 V). Broadened MoS_2 (JCPDS #37-1492), rGO (JCPDS #01-0646), Mo (JCPDS #01-1207), and Na_2S (JCPDS #65-0525) peaks were observed in the sodiated electrode.[68−70]

the current density was brought back to 25 mA g^{-1} after 15 cycles. On further increasing the current density to 200 mA g^{-1}, 72% (173 mAh g^{-1}) of the initial stable capacity was retained. Again, when the current density was brought back to the initial 25 mA g^{-1}, the electrode recovered 87% of its capacity and remained stable for another five cycles. It is remarkable that, even at 200 mA g^{-1}, the electrode had a stable charge/discharge cycle with no abnormalities, which suggests the improved mechanical stability of this interleaved architecture. Summary of the electrochemical data is presented in Table S3.

Further, to check the integrity of the electrode specimen, the cells were disassembled and the electrode was recovered for further characterization. Supporting Information Figure S10 shows the digital photographs (a−e), low-resolution (f−j), and high-resolution (k−o) SEM images of the dissembled cells after 20 cycles. No evidence of surface cracks, volume change, or physical imperfections could be observed in the SEM image, suggesting high mechanical/structural strength of the MoS_2/rGO composite paper. In all cases, the evidence of formation of a thin layer covering the electrode surface, possibly the SEI layer, could be observed. The contamination in the specimen, indicated by the arrows, is from the residue of glass separator fibers. Also, these anodes may have been exposed to air during the transfer process, resulting in oxidation of Na species,

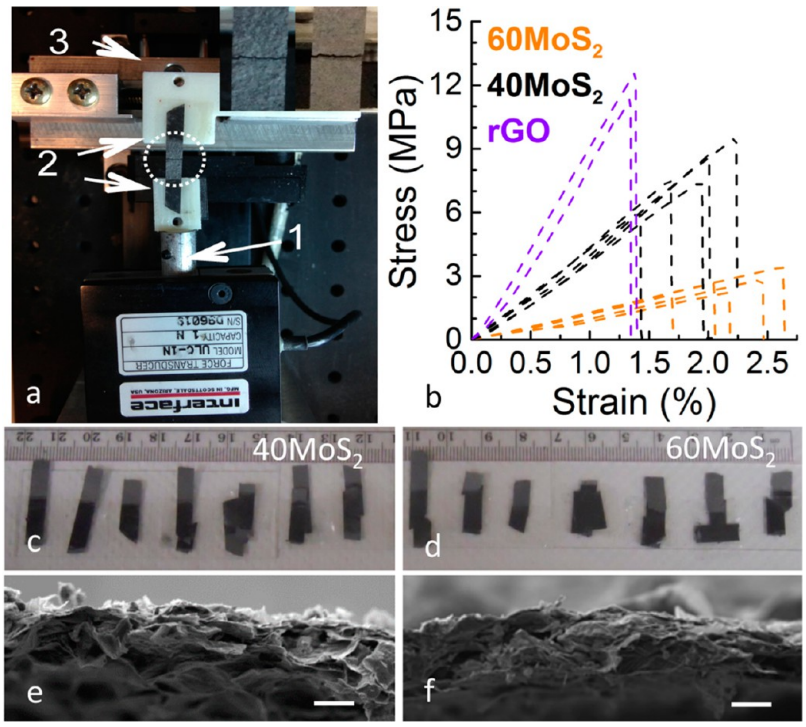

Figure 5. (a) Tensile test setup (1, load cell, fixed; 2, clamps, top clamp not shown; 3, computer-controlled movable translation stage) with sample after fracture from loading (inset shows zoomed-in view of two such specimens). (b) Engineering stress−strain plot for rGO, 40MoS_2, and 60MoS_2 free-standing papers. Photographic image of (c) 40MoS_2 and (d) 60MoS_2 paper tested in this study. (e,f) Corresponding SEM cross-sectional images showing the fractured surface. The scale bar is 20 μm.

which appeared as bright spots in the images (due to its nonconducting nature). Supporting Information Figure S11 shows the images obtained by EDX mapping of the electrode surface. Table S2 shows the atomic weight percent of various elements detected during the EDX mapping. A high percentage of sodium (19.46 atom %) was observed on the electrode surface, which is generally attributed to formation of a SEI layer during the electrochemical cycling process. Even higher percentage of surface oxygen (41.46 atom %) was observed, which may have come from oxidation of intercalated sodium metal. Further analysis involved disassembling 60MoS_2 cell after first discharge cycle. TEM images in Figure 4a show degradation of MoS_2 sheets and possible amorphization (ring-like SAED pattern).[67] Complementing results were observed in XRD and XPS analysis of the fully sodiated electrode, as shown in Figure 4b and Supporting Information Figure S12, respectively. Broad Mo peak and Na−S peaks could be identified in both XRD (Mo at 29°, Na−S at 72° 2θ) and XPS (Mo at 231 eV, Na−S at 160.6 eV) spectra. Also, the primary MoS_2 peak at 14° 2θ (002) appeared broadened, further indicating degradation of MoS_2 structure, most likely due to a conversion-type reaction with Na ions.[68−70]

On the basis of the voltage profiles, differential capacity plots, GITT cycling data, and post-cycling analysis, we predict the mechanism of Na ion's reaction with the MoS_2/graphene composite to be a combination of intercalation and conversion-type reaction that is generally observed in Li/TMDC[34] and cathodes for Na-ion batteries.[71,72] Supporting Information Figure S13 shows an idealized rGO/MoS_2 structure (in reality, however, the acid-treated MoS_2 sheets are wrapped by much larger rGO sheets) to illustrate the predicted reaction mechanism in the 2.0 to 0.1 V range. Step 1 is seen as a combination of Na intercalation reaction into the ordered MoS_2 (~0.9 V) and later into the disordered Na_xMoS_2 layers (~0.8 V). Step 2 represents the conversion reaction resulting in breakdown of MoS_2 into Mo and Na_2S, as can be seen in the TEM (Figure 4a), XRD (Figure 4b), and XPS data from the fully sodiated cell in Supporting Information Figure S12 (further confirmed by the lower voltage plateau at ~0.12 V that was not observed in the discharge of rGO electrode, Supporting Information Figure S7a). A more detailed analysis may be obtained from *in situ* synchrotron powder diffraction[73] and spectroscopy studies similar to those demonstrated by Grey's group on LIBs.[74,75]

The tensile strength and strain to failure are important parameters for any flexible battery electrode. Therefore, the rGO, 40MoS_2, and 60MoS_2 papers were subjected to static uniaxial tensile testing in a custom-built setup (see Methods, Materials, and Instrumentation and Figure 5a). As can be seen, the specimen strip is secured on one end by a computer-controlled movable stage, while the other end is fixed to a load cell, which in turn is fixed to an immovable stage. Engineering stress−strain plots derived from load−displacement

TABLE 1. Summary of Tensile Test Data for rGO, 40MoS_2, and 60MoS_2 Free-Standing Composite Papers

specimen	modulus (MPa)	tensile strength (MPa)	failure strain (%)
rGO	897.86 ± 18.86	12.57 ± 0.13	1.4 ± 0.014
	874.62 ± 18.37	11.37 ± 0.12	1.3 ± 0.014
40MoS_2	427.03 ± 8.97	9.48 ± 0.1	2.22 ± 0.023
	434.5 ± 9.12	8.69 ± 0.09	2 ± 0.021
	386.01 ± 8.11	7.45 ± 0.08	1.93 ± 0.02
	450 ± 9.45	7.56 ± 0.08	1.68 ± 0.017
	424.8 ± 8.92	6.06 ± 0.06	1.43 ± 0.015
60MoS_2	130.8 ± 2.75	3.44 ± 0.04	2.63 ± 0.028
	115.92 ± 2.43	2.84 ± 0.03	2.45 ± 0.026
	102.76 ± 2.16	2.23 ± 0.02	2.17 ± 0.023
	131.22 ± 2.76	2.69 ± 0.03	2.05 ± 0.021
	125.85 ± 2.64	2.13 ± 0.02	1.69 ± 0.018

data are shown in Figure 5b. 40MoS_2 showed higher fracture strength and modulus (approximately 7.8 and 424 MPa) than 60MoS_2 (approximately 2.1 and 120 MPa) composite paper. On comparison, rGO had fracture strength and modulus of approximately 12 and 885 MPa, respectively. The tensile strength of rGO paper is comparable to those reported by Nyugen's group involving *in situ* reduced GO papers.[76] These values are, however, much lower than GO papers, but this is hardly surprising considering that our papers were annealed at high temperatures (500 °C for 2 h and 900 °C for 5 min) and the mechanical strength of GO generally decreases with increasing annealing temperatures caused by release of oxygen groups that disturb the structure of the paper, resulting in a highly crumpled configuration.[77] The strain to failure was higher in the case of the 60MoS_2 specimen, reaching values in excess of approximately 2%. A total of five specimens were tested for 40MoS_2 and 60MoS_2 paper, each that are shown in the photographic image in Figure 5c,d, respectively. Data are summarized in Table 1. Figure 5e,f is the corresponding SEM images of the fractured edge for 40MoS_2 and 60MoS_2, respectively. The edge was observed to be more regular and smooth for 60MoS_2 than for 40MoS_2. The variation in strain to failure for the composite specimen is attributed partially to the likely inhomogeneity in the specimens (large size of the paper and higher loading 4 mg cm^{-2}) and crumpled nature of the rGO layers. Subsequently, combined with observations in SEM images, 60MoS_2 had even larger variation in failure strain as the more slippery MoS_2 sheets can slide better than crumpled rGO sheets.

CONCLUSION

We have demonstrated synthesis of a composite-layered paper consisting of acid-exfoliated MoS_2 nanoflakes in an rGO matrix. Mechanical tests involving static uniaxial tension reveal mechanical strength that was approximately 2−3 MPa and high failure strain (approximately 2%) in these materials. Further, the composite paper was directly utilized as counter electrode in Na-ion battery half-cell, and its performance was evaluated as a potential anode for use in a Na-ion battery full cell. These tests revealed high first cycle electrochemical capacity of 338 mAh g^{-1} with respect to total weight of the electrode with excellent cyclability of Na ions. This study provides the first experimental evidence of reversible electrochemical storage of Na in a layered self-standing MoS_2 composite electrode at room temperatures and is expected to open new avenues for use of large-area free-standing binder-free flexible electrodes for rechargeable battery applications.

METHODS, MATERIALS, AND INSTRUMENTATION

The ζ-potential surface measurements were carried out on a ZetaPlus ζ-potential analyzer (Brookhaven's Inst. Corp.). The effect of ionic concentration on the potential measured is minimized by using a low concentration of basic (0.01 M NaOH) solution for controlling the pH. Scanning electron microscopy (SEM) of the synthesized material was carried out on a Carl Zeiss EVO MA10 system with incident voltage of 5 to 30 kV. TEM images were digitally acquired by use of a Phillips CM100 operated at 100 KV. Material characterization was made using an X-ray diffractometer (XRD) operating at room temperature with nickel-filtered Cu Kα radiation (λ = 1.5418 Å). Thermogravimetric analysis was performed using Shimadzu 50 TGA (limited to 800 °C). Samples weighing ∼2.5 mg were heated in a platinum pan at a rate of 10 °C min^{-1} in air flowing at 20 mL min^{-1}. Raman spectra were measured using a LabRAM ARMIS Raman spectrometer using 633 nm laser excitation (laser power of 17 mW) as the light source. The surface chemical composition was studied by X-ray photoelectron spectroscopy (XPS, PHI Quantera SXM) using monochromatic Al Kα radiation. Static uniaxial in-plane tensile tests were conducted in a simple test setup. The sample strip is secured on one end by a computer-controlled movable stage (M-111.2DG from PI), while the other end is fixed to a 1N load cell (ULC-1N Interface), which in turn is fixed to an immovable stage. All tensile tests were conducted in controlled strain rate mode with a strain rate of 0.2% min^{-1}. The samples were cut with a razor into rectangular strips of approximately 5 × 15 mm^2 for testing without further modification. Electrical conductivity measurements were carried out by use of a four-point probe setup and Keithley 2636A (Cleveland, OH) dual channel sourcemeter in the ohmic region. Electrochemical cycling of the assembled cells was carried out using multichannel battery test equipment (Arbin-BT2000, Austin, TX) at atmospheric conditions.

Preparation of Graphene Oxide. Sodium nitrate (99.2%), potassium permanganate (99.4%), sulfuric acid (96.4%), hydrogen peroxide (31.3% solution in water), hydrochloric acid (30% solution in water), and methanol (99.9%) were purchased from Fisher Scientific. All materials were used as received without further purification. Modified Hummer's method was used to make graphene oxide.[49] Concentrated H_2SO_4 (130 mL) was added to a mixture of graphite flakes (3 g) and $NaNO_3$ (1.5 g). The mixture was cooled using an ice bath. $KMnO_4$ was added slowly to this mixture. The mixture was stirred for 12 h at 50 °C. Then it was quenched with water (400 mL) with 30% H_2O_2 (3 mL) while in an ice bath such that the temperature does not go beyond 20 °C. The remaining material was then washed in succession with 200 mL of water twice, 200 mL of 30% HCl, and 200 mL of ethanol. The material remaining after these extended washes is coagulated with 200 mL of ether and filtered through

a paper filter. The filtrate is dried overnight to obtain dry graphene oxide.

Preparation of Exfoliated or Acid-Treated MoS_2 Flakes. MoS_2 powder (2 mg mL^{-1}, 99%, Sigma Aldrich) was sonicated for 30 min in concentrated chlorosulfonic acid (superacid, 99%, Sigma Aldrich), and the non-exfoliated sheets were allowed to settle. Please note that the superacid was very slowly added to the MoS_2 powder in an argon-filled glovebox (dew point −50 °C). The solution was then carefully quenched in 1.0 L of distilled water (done with extreme caution in a glovebox). Additional dilution with DI water was done to reduce the solution acidity. The solution was then dried in a conventional oven to obtain dry superacid-treated MoS_2 (MoS_2-SA).

Preparation of Reduced Graphene Oxide and MoS_2 Composite Paper. The composite papers were prepared in two sizes: 1.8 and 6.25 in. diameters. Small size papers were prepared to save material costs and time (since coin cells could only accommodate a specimen approximately 1.4 cm in diameter). Large size paper was prepared only for the 60MoS_2 electrode since it was the best performing specimen and most challenging to prepare considering the high percentage of MoS_2 in it.

Small size papers: 15 mg of GO and varying weight percent of MoS_2 (prepared from the procedure stated above) were mixed together in 1:1 (v/v) water and isopropyl alcohol solution. The mixture was then sonicated for 60 min (Branson Sonifier S-450A, 400 W). The composite suspension was then filtered by a vacuum filtration process through a 47 mm diameter 10 μm pore-sized filter membrane (HPLC grade, Millipore). MoS_2/GO composite paper thus obtained was dried in an oven at 70 °C overnight and subsequently reduced at 500 °C for 2 h and 900 °C for 5 min in argon atmosphere. The samples were labeled as rGO, 20MoS_2, 40MoS_2, and 60MoS_2 for pristine rGO paper and rGO with 20, 40, and 60% of MoS_2 in the total weight of the paper, respectively. The 60MoS_2-raw paper was synthesized with as-obtained MoS_2 and GO, following the process stated above. Later, the large-area paper with 60MoS_2 composition (approximately 6.25 in. diameter, cut into rectangular strip shown in Figure 2b) was prepared following a similar procedure by use of a Büchner funnel with a polypropylene filter paper (Celgard).

Coin Cell/Battery Assembly. For electrochemical testing, 2032 half-coin cells were made by punching 14.3 mm diameter out of the composite paper for use as working electrode. Then, 1 M $NaClO_4$ (Alfa Aesar) in (1:1 v/v) dimethyl carbonate/ethylene carbonate served as the electrolyte. A 25 μm thick (19 mm diameter) glass separator soaked in electrolyte was placed between the working electrode and pure Na metal (14.3 mm diameter, 75 μm thick) counter electrode. Washer, spring, and a top casing were placed on top to complete the assembly before crimping. The assembled cells were tested using a multichannel BT2000 Arbin test unit sweeping between 2.25 V to 10 mV *vs* Na/Na^+. *C* rate performance of the best performing electrode material (60MoS_2) was tested in the voltage range from 2.25 to 0.1 V *vs* Na/Na^+ using the following cycle schedule: Na^+ was inserted at 100 mA g^{-1}, while the extraction was performed at current densities of 25, 50, 100, 25, 150, 200, and 25 mA g^{-1} for five cycles consecutively.

Conflict of Interest: The authors declare the following competing financial interest(s): G. Singh and L. David have filed for a provisional patent: U.S. Provisional Patent Application 61/862,289; ROBUST MoS2/GRAPHENE COMPOSITE FOR NA+ BATTERY APPLICATION; Docket No. 45573-PRO.

Acknowledgment. L.D. would like to thank Erin Black for assistance with specimen preparation. We thank Professor Kevin Lease and Nasim Rahmani (K-State) for access to their lab for mechanical testing. Thanks are also due to Dr. Andras Kis (EPFL) and Dr. Scott Bunch (BU) for visit to K-State and useful discussions related to layered materials. G.S. thanks Michele Anderson (ONR) for encouragement to pursue this research.

Supporting Information Available: TEM images, SAED pattern, SEM images, elemental mapping data, X-ray photoelectron spectroscopy data, X-ray diffraction data, Raman spectroscopy data, GITT data for rGO and 60MoS_2 electrodes, voltage profiles, post-electrochemical analysis, and summary of electrical conductivity data. This material is available free of charge *via* the Internet at http://pubs.acs.org.

REFERENCES AND NOTES

1. Armand, M.; Tarascon, J. M. Building Better Batteries. *Nature* **2008**, *451*, 652–657.
2. Manthiram, A.; Fu, Y.; Su, Y. S. In Charge of the World: Electrochemical Energy Storage. *J. Phys. Chem. Lett.* **2013**, *4*, 1295–1297.
3. Saravanan, K.; Mason, C. W.; Rudola, A.; Wong, K. H.; Balaya, P. The First Report on Excellent Cycling Stability and Superior Rate Capability of $Na_3V_2(PO_4)_3$ for Sodium Ion Batteries. *Adv. Energy Mater.* **2013**, *3*, 444–450.
4. Tarascon, J. M. Is Lithium the New Gold?. *Nat. Chem.* **2010**, *2*, 510.
5. Ellis, B. L.; Makahnouk, W. R. M.; Makimura, Y.; Toghill, K.; Nazar, L. F. A Multifunctional 3.5 V Iron-Based Phosphate Cathode for Rechargeable Batteries. *Nat. Mater.* **2007**, *6*, 749–753.
6. Kim, D.; Kang, S. H.; Slater, M.; Rood, S.; Vaughey, J. T.; Karan, N.; Balasubramanian, M.; Johnson, C. S. Enabling Sodium Batteries Using Lithium-Substituted Sodium Layered Transition Metal Oxide Cathodes. *Adv. Energy Mater.* **2011**, *1*, 333–336.
7. Cao, Y.; Xiao, L.; Wang, W.; Choi, D.; Nie, Z.; Yu, J.; Saraf, L. V.; Yang, Z.; Liu, J. Reversible Sodium Ion Insertion in Single Crystalline Manganese Oxide Nanowires with Long Cycle Life. *Adv. Mater.* **2011**, *23*, 3155–3160.
8. Ellis, B. L.; Nazar, L. F. Sodium and Sodium-Ion Energy Storage Batteries. *Curr. Opin. Solid State Mater. Sci.* **2012**, *16*, 168–177.
9. Chevrier, V. L.; Ceder, G. Challenges for Na-Ion Negative Electrodes. *J. Electrochem. Soc.* **2011**, *158*, A1011–A1014.
10. Lin, Y. M.; Abel, P. R.; Gupta, A.; Goodenough, J. B.; Heller, A.; Mullins, C. B. Sn−Cu Nanocomposite Anodes for Rechargeable Sodium-Ion Batteries. *ACS Appl. Mater. Interfaces* **2013**, *5*, 8273–8277.
11. Darwiche, A.; Marino, C.; Sougrati, M. T.; Fraisse, B.; Stievano, L.; Monconduit, L. Better Cycling Performances of Bulk Sb in Na-Ion Batteries Compared to Li-Ion Systems: An Unexpected Electrochemical Mechanism. *J. Am. Chem. Soc.* **2012**, *134*, 20805–20811.
12. Xiao, L.; Cao, Y.; Xiao, J.; Wang, W.; Kovarik, L.; Nie, Z.; Liu, J. High Capacity, Reversible Alloying Reactions in SnSb/C Nanocomposites for Na-Ion Battery Applications. *Chem. Commun.* **2012**, *48*, 3321–3323.
13. Qian, J.; Chen, Y.; Wu, L.; Cao, Y.; Ai, X.; Yang, H. High Capacity Na-Storage and Superior Cyclability of Nanocomposite Sb/C Anode for Na-Ion Batteries. *Chem. Commun.* **2012**, *48*, 7070–7072.
14. Qian, J.; Wu, X.; Cao, Y.; Ai, X.; Yang, H. High Capacity and Rate Capability of Amorphous Phosphorus for Sodium Ion Batteries. *Angew. Chem., Int. Ed.* **2013**, *52*, 4633–4636.
15. Kim, Y.; Park, Y.; Choi, A.; Choi, N. S.; Kim, J.; Lee, J.; Ryu, J. H.; Oh, S. M.; Lee, K. T. An Amorphous Red Phosphorus/Carbon Composite as a Promising Anode Material for Sodium Ion Batteries. *Adv. Mater.* **2013**, *25*, 3045–3049.
16. Xiong, H.; Slater, M. D.; Balasubramanian, M.; Johnson, C. S.; Rajh, T. Amorphous TiO_2 Nanotube Anode for Rechargeable Sodium Ion Batteries. *J. Phys. Chem. Lett.* **2011**, *2*, 2560–2565.
17. Zhu, H.; Jia, Z.; Chen, Y.; Weadock, N.; Wan, J.; Vaaland, O.; Han, X.; Li, T.; Hu, L. Tin Anode for Sodium-Ion Batteries Using Natural Wood Fiber as a Mechanical Buffer and Electrolyte Reservoir. *Nano Lett.* **2013**, *13*, 3093–3100.
18. Zhu, Y.; Han, X.; Xu, Y.; Liu, Y.; Zheng, S.; Xu, K.; Hu, L.; Wang, C. Electrospun Sb/C Fibers for a Stable and Fast Sodium-Ion Battery Anode. *ACS Nano* **2013**, *7*, 6378–6386.
19. Stevens, D. A.; Dahn, J. R. High Capacity Anode Materials for Rechargeable Sodium-Ion Batteries. *J. Electrochem. Soc.* **2000**, *147*, 1271–1273.
20. Alcántara, R.; Jiménez-Mateos, J. M.; Lavela, P.; Tirado, J. L. Carbon Black: A Promising Electrode Material for Sodium-Ion Batteries. *Electrochem. Commun.* **2001**, *3*, 639–642.

21. Alcántara, R.; Jiménez Mateos, J. M.; Tirado, J. L. Negative Electrodes for Lithium- and Sodium-Ion Batteries Obtained by Heat-Treatment of Petroleum Cokes below 1000°C. *J. Electrochem. Soc.* **2002**, *149*, A201–A205.
22. Komaba, S.; Murata, W.; Ishikawa, T.; Yabuuchi, N.; Ozeki, T.; Nakayama, T.; Ogata, A.; Gotoh, K.; Fujiwara, K. Electrochemical Na Insertion and Solid Electrolyte Interphase for Hard-Carbon Electrodes and Application to Na-Ion Batteries. *Adv. Funct. Mater.* **2011**, *21*, 3859–3867.
23. Cao, Y.; Xiao, L.; Sushko, M. L.; Wang, W.; Schwenzer, B.; Xiao, J.; Nie, Z.; Saraf, L. V.; Yang, Z.; Liu, J. Sodium Ion Insertion in Hollow Carbon Nanowires for Battery Applications. *Nano Lett.* **2012**, *12*, 3783–3787.
24. Palacin, M. R. Recent Advances in Rechargeable Battery Materials: A Chemist's Perspective. *Chem. Soc. Rev.* **2009**, *38*, 2565–2575.
25. Ponrouch, A.; Goñi, A. R.; Palacín, M. R. High Capacity Hard Carbon Anodes for Sodium Ion Batteries in Additive Free Electrolyte. *Electrochem. Commun.* **2013**, *27*, 85–88.
26. Liu, H.; Su, D.; Zhou, R.; Sun, B.; Wang, G.; Qiao, S. Z. Highly Ordered Mesoporous MoS_2 with Expanded Spacing of the (002) Crystal Plane for Ultrafast Lithium Ion Storage. *Adv. Energy Mater.* **2012**, *2*, 970–975.
27. Tepavcevic, S.; Xiong, H.; Stamenkovic, V. R.; Zuo, X.; Balasubramanian, M.; Prakapenka, V. B.; Johnson, C. S.; Rajh, T. Nanostructured Bilayered Vanadium Oxide Electrodes for Rechargeable Sodium-Ion Batteries. *ACS Nano* **2011**, *6*, 530–538.
28. Hu, Y.; Li, X.; Lushington, A.; Cai, M.; Geng, D.; Banis, M. N.; Li, R.; Sun, X. Fabrication of MoS_2-Graphene Nanocomposites by Layer-by-Layer Manipulation for High-Performance Lithium Ion Battery Anodes. *ECS J. Solid State Sci. Technol.* **2013**, *2*, M3034–M3039.
29. Xiao, J.; Wang, X.; Yang, X. Q.; Xun, S.; Liu, G.; Koech, P. K.; Liu, J.; Lemmon, J. P. Electrochemically Induced High Capacity Displacement Reaction of PEO/MoS_2/Graphene Nanocomposites with Lithium. *Adv. Funct. Mater.* **2011**, *21*, 2840–2846.
30. Zhou, X.; Wan, L. J.; Guo, Y. G. Facile Synthesis of MoS_2@CMK-3 Nanocomposite as an Improved Anode Material for Lithium-Ion Batteries. *Nanoscale* **2012**, *4*, 5868–5871.
31. Hwang, H.; Kim, H.; Cho, J. MoS_2 Nanoplates Consisting of Disordered Graphene-like Layers for High Rate Lithium Battery Anode Materials. *Nano Lett.* **2011**, *11*, 4826–4830.
32. Chang, K.; Chen, W. L-Cysteine-Assisted Synthesis of Layered MoS_2/Graphene Composites with Excellent Electrochemical Performances for Lithium Ion Batteries. *ACS Nano* **2011**, *5*, 4720–4728.
33. Zhao, X.; Hayner, C. M.; Kung, M. C.; Kung, H. H. Flexible Holey Graphene Paper Electrodes with Enhanced Rate Capability for Energy Storage Applications. *ACS Nano* **2011**, *5*, 8739–8749.
34. Cabana, J.; Monconduit, L.; Larcher, D.; Rosa Palacin, M. Beyond Intercalation-Based Li-Ion Batteries: The State of the Art and Challenges of Electrode Materials Reacting through Conversion Reactions. *Adv. Mater.* **2010**, *22*, E170–E192.
35. Ji, H.; Zhang, L.; Pettes, M. T.; Li, H.; Chen, S.; Shi, L.; Piner, R.; Ruoff, R. S. Ultrathin Graphite Foam: A Three-Dimensional Conductive Network for Battery Electrodes. *Nano Lett.* **2012**, *12*, 2446–2451.
36. Hwang, H.; Kim, H.; Cho, J. MoS_2 Nanoplates Consisting of Disordered Graphene-like Layers for High Rate Lithium Battery Anode Materials. *Nano Lett.* **2011**, *11*, 4826–4830.
37. Chhowalla, M.; Shin, H. S.; Eda, G.; Li, L. J.; Loh, K. P.; Zhang, H. The Chemistry of Two-Dimensional Layered Transition Metal Dichalcogenide Nanosheets. *Nat. Chem.* **2013**, *5*, 263–275.
38. Ge, P.; Fouletier, M. Electrochemical Intercalation of Sodium in Graphite. *Solid State Ionics* **1988**, *28–30*, 1172–1175.
39. Stevens, D. A.; Dahn, J. R. The Mechanisms of Lithium and Sodium Insertion in Carbon Materials. *J. Electrochem. Soc.* **2001**, *148*, A803–A811.
40. Asher, R. C. A Lamellar Compound of Sodium and Graphite. *J. Inorg. Nucl. Chem.* **1959**, *10*, 238–249.
41. Hu, L.; Choi, J. W.; Yang, Y.; Jeong, S.; La Mantia, F.; Cui, L. F.; Cui, Y. Highly Conductive Paper for Energy-Storage Devices. *Proc. Natl. Acad. Sci. U.S.A.* **2009**, *106*, 21490–21494.
42. Cui, L. F.; Hu, L.; Choi, J. W.; Cui, Y. Light-Weight Free-Standing Carbon Nanotube-Silicon Films for Anodes of Lithium Ion Batteries. *ACS Nano* **2010**, *4*, 3671–3678.
43. Wang, D.; Kou, R.; Choi, D.; Yang, Z.; Nie, Z.; Li, J.; Saraf, L. V.; Hu, D.; Zhang, J.; Graff, G. L.; *et al.* Ternary Self-Assembly of Ordered Metal Oxide–Graphene Nanocomposites for Electrochemical Energy Storage. *ACS Nano* **2010**, *4*, 1587–1595.
44. Li, N.; Chen, Z.; Ren, W.; Li, F.; Cheng, H. M. Flexible Graphene-Based Lithium Ion Batteries with Ultrafast Charge and Discharge Rates. *Proc. Natl. Acad. Sci. U.S.A.* **2012**, *109*, 17360–17365.
45. Zhao, X.; Hayner, C. M.; Kung, M. C.; Kung, H. H. In-Plane Vacancy-Enabled High-Power Si–Graphene Composite Electrode for Lithium-Ion Batteries. *Adv. Energy Mater.* **2011**, *1*, 1079–1084.
46. Abouimrane, A.; Compton, O. C.; Amine, K.; Nguyen, S. T. Non-annealed Graphene Paper as a Binder-Free Anode for Lithium-Ion Batteries. *J. Phys. Chem. C* **2010**, *114*, 12800–12804.
47. Koo, M.; Park, K. I.; Lee, S. H.; Suh, M.; Jeon, D. Y.; Choi, J. W.; Kang, K.; Lee, K. J. Bendable Inorganic Thin-Film Battery for Fully Flexible Electronic Systems. *Nano Lett.* **2012**, *12*, 4810–4816.
48. Magasinski, A.; Dixon, P.; Hertzberg, B.; Kvit, A.; Ayala, J.; Yushin, G. High-Performance Lithium-Ion Anodes Using a Hierarchical Bottom-Up Approach. *Nat. Mater.* **2010**, *9*, 353–358.
49. Hummers, W. S.; Offeman, R. E. Preparation of Graphitic Oxide. *J. Am. Chem. Soc.* **1958**, *80*, 1339–1339.
50. Bhandavat, R.; David, L.; Singh, G. Synthesis of Surface-Functionalized WS_2 Nanosheets and Performance as Li-Ion Battery Anodes. *J. Phys. Chem. Lett.* **2012**, *3*, 1523–1530.
51. Lotya, M.; Hernandez, Y.; King, P. J.; Smith, R. J.; Nicolosi, V.; Karlsson, L. S.; Blighe, F. M.; De, S.; Wang, Z.; McGovern, I. T.; *et al.* Liquid Phase Production of Graphene by Exfoliation of Graphite in Surfactant/Water Solutions. *J. Am. Chem. Soc.* **2009**, *131*, 3611–3620.
52. Coleman, J. N.; Lotya, M.; O'Neill, A.; Bergin, S. D.; King, P. J.; Khan, U.; Young, K.; Gaucher, A.; De, S.; Smith, R. J.; *et al.* Two-Dimensional Nanosheets Produced by Liquid Exfoliation of Layered Materials. *Science* **2011**, *331*, 568–571.
53. Bertrand, P. A. Surface-Phonon Dispersion of MoS_2. *Phys. Rev. B* **1991**, *44*, 5745–5749.
54. Lee, C.; Yan, H.; Brus, L. E.; Heinz, T. F.; Hone, J.; Ryu, S. Anomalous Lattice Vibrations of Single- and Few-Layer MoS_2. *ACS Nano* **2010**, *4*, 2695–2700.
55. Chen, J. M.; Wang, C. S. Second Order Raman Spectrum of MoS_2. *Solid State Commun.* **1974**, *14*, 857–860.
56. Windom, B.; Sawyer, W. G.; Hahn, D. A Raman Spectroscopic Study of MoS_2 and MoO_3: Applications to Tribological Systems. *Tribol. Lett.* **2011**, *42*, 301–310.
57. Stacy, A. M.; Hodul, D. T. Raman Spectra of IVB and VIB Transition Metal Disulfides Using Laser Energies near the Absorption Edges. *J. Phys. Chem. Solids* **1985**, *46*, 405–409.
58. Frey, G. L.; Tenne, R.; Matthews, M. J.; Dresselhaus, M. S.; Dresselhaus, G. Raman and Resonance Raman Investigation of MoS_2 Nanoparticles. *Phys. Rev. B* **1999**, *60*, 2883–2892.
59. Jiménez Sandoval, S.; Yang, D.; Frindt, R. F.; Irwin, J. C. Raman Study and Lattice Dynamics of Single Molecular Layers of MoS_2. *Phys. Rev. B* **1991**, *44*, 3955–3962.
60. Frey, G. L.; Reynolds, K. J.; Friend, R. H.; Cohen, H.; Feldman, Y. Solution-Processed Anodes from Layer-Structure Materials for High-Efficiency Polymer Light-Emitting Diodes. *J. Am. Chem. Soc.* **2003**, *125*, 5998–6007.
61. Du, G.; Guo, Z.; Wang, S.; Zeng, R.; Chen, Z.; Liu, H. Superior Stability and High Capacity of Restacked Molybdenum Disulfide as Anode Material for Lithium Ion Batteries. *Chem. Commun.* **2010**, *46*, 1106–1108.

62. Visic, B.; Dominko, R.; Gunde, M. K.; Hauptman, N.; Skapin, S. D.; Remskar, M. Optical Properties of Exfoliated MoS_2 Coaxial Nanotubes: Analogues of Graphene. *Nanoscale Res. Lett.* **2011**, *6*, 1–6.
63. Putz, K. W.; Compton, O. C.; Palmeri, M. J.; Nguyen, S. T.; Brinson, L. C. High-Nanofiller-Content Graphene Oxide−Polymer Nanocomposites *via* Vacuum-Assisted Self-Assembly. *Adv. Funct. Mater.* **2010**, *20*, 3322–3329.
64. Cunningham, G.; Lotya, M.; McEvoy, N.; Duesberg, G. S.; van der Schoot, P.; Coleman, J. N. Percolation Scaling in Composites of Exfoliated MoS_2 Filled with Nanotubes and Graphene. *Nanoscale* **2012**, *4*, 6260–6264.
65. Stauffer, D.; Aharony, A. *Introduction to Percolation Theory*; Taylor & Francis: London, 1985.
66. Wang, C.; Kakwana, I.; Appleby, A. J.; Little, F. E. *In Situ* Investigation of Electrochemical Lithium Intercalation into Graphite Powder. *J. Electroanal. Chem.* **2000**, *489*, 55–67.
67. Firmiano, E. G. S.; Cordeiro, M. A. L.; Rabelo, A. C.; Dalmaschio, C. J.; Pinheiro, A. N.; Pereira, E. C.; Leite, E. R. Graphene Oxide as a Highly Selective Substrate To Synthesize a Layered MoS_2 Hybrid Electrocatalyst. *Chem. Commun.* **2012**, *48*, 7687–7689.
68. Hariharan, S.; Saravanan, K.; Balaya, P. α-MoO_3: A High Performance Anode Material for Sodium-Ion Batteries. *Electrochem. Commun.* **2013**, *31*, 5–9.
69. Das, S. K.; Mallavajula, R.; Jayaprakash, N.; Archer, L. A. Self-Assembled MoS_2-Carbon Nanostructures: Influence of Nanostructuring and Carbon on Lithium Battery Performance. *J. Mater. Chem.* **2012**, *22*, 12988–12992.
70. Yang, L.; Yu, H.; Xu, L.; Ma, Q.; Qian, Y. Sulfur-Assisted Synthesis of Nitride Nanocrystals. *Dalton Trans.* **2010**, *39*, 2855–2860.
71. Kim, J. S.; Ahn, H. J.; Ryu, H. S.; Kim, D. J.; Cho, G. B.; Kim, K. W.; Nam, T. H.; Ahn, J. H. The Discharge Properties of Na/Ni_3S_2 Cell at Ambient Temperature. *J. Power Sources* **2008**, *178*, 852–856.
72. Park, J.; Kim, J. S.; Park, J. W.; Nama, T. H.; Kim, K. W.; Ahn, J. H.; Wang, G.; Ahn, H. J. Discharge Mechanism of MoS_2 for Sodium Ion Battery: Electrochemical Measurements and Characterization. *Electrochim. Acta* **2013**, *92*, 427–432.
73. Misra, S.; Liu, N.; Nelson, J.; Hong, S. S.; Cui, Y.; Toney, M. F. *In Situ* X-ray Diffraction Studies of (De)lithiation Mechanism in Silicon Nanowire Anodes. *ACS Nano* **2012**, *6*, 5465–5473.
74. Bhattacharyya, R.; Key, B.; Chen, H.; Best, A. S.; Hollenkamp, A. F.; Grey, C. P. *In Situ* NMR Observation of the Formation of Metallic Lithium Microstructures in Lithium Batteries. *Nat. Mater.* **2010**, *9*, 504–510.
75. Yamakawa, N.; Jiang, M.; Key, B.; Grey, C. P. A Study of the Lithium Conversion Mechanism of Iron Fluoride in a Li Ion Battery, by Using Solid State NMR, XRD and PDF Analysis Studies. *J. Am. Chem. Soc.* **2009**, *131*, 10525–10536.
76. Compton, O. C.; Dikin, D. A.; Putz, K. W.; Brinson, L. C.; Nguyen, S. T. Electrically Conductive "Alkylated" Graphene Paper *via* Chemical Reduction of Amine-Functionalized Graphene Oxide Paper. *Adv. Mater.* **2010**, *22*, 892–896.
77. Compton, O. C.; Nguyen, S. T. Graphene Oxide, Highly Reduced Graphene Oxide, and Graphene: Versatile Building Blocks for Carbon-Based Materials. *Small* **2010**, *6*, 711–723.